

Drift Turbulence, Particle Transport, and Anomalous Dissipation at the Reconnecting Magnetopause

A. Le,¹ W. Daughton,¹ O. Ohia,¹ L.-J. Chen,² Y.-H. Liu,³ and S. Wang²

¹*Los Alamos National Laboratory, Los Alamos, New Mexico 87545, USA*

²*University of Maryland, College Park, College Park,*

Maryland 20742 USA and NASA Goddard Space

Flight Center, Greenbelt, Maryland 20771 USA

³*Dartmouth College, Hanover, New Hampshire 03755, USA*

Abstract

Using fully kinetic 3D simulations, the reconnection dynamics of asymmetric current sheets are examined at the Earth's magnetopause. The plasma parameters are selected to match MMS magnetopause diffusion region crossings with guide fields of 0.1, 0.4, and 1 of the reconnecting magnetosheath field. In each case, strong drift-wave fluctuations are observed in the lower-hybrid frequency range at the steep density gradient across the magnetospheric separatrix. These fluctuations give rise to cross-field particle transport for both electron and ions. In addition, this turbulent mixing leads to significantly enhanced electron parallel heating in comparison to 2D simulations. We study three different methods of quantifying the anomalous dissipation produced by the drift fluctuations, based on spatial averaging, temporal averaging, and temporal averaging followed by integrating along magnetic field lines. Comparing the different methods reveals complications that make identifying and measuring the anomalous dissipation unclear. Nevertheless, the anomalous dissipation from short wavelength drift fluctuations appears weak for each case, and the reconnection rates observed in 3D are nearly the same as in 2D models. The 3D simulations feature a number of interesting new features that are consistent with recent MMS observations, including cold beams of sheath electrons that penetrate into the hotter magnetospheric inflow, the related observation of decreasing temperature in regions of increasing total density, and an effective turbulent diffusion coefficient that agrees with quasi-linear theoretical predictions.

I. INTRODUCTION

Magnetic reconnection plays a central role in the dynamics of the magnetosphere, the solar wind, the solar corona, and a variety of other space plasmas where particle collisions are negligible [1, 2]. In these collisionless plasmas, kinetic effects ultimately control the evolution of reconnecting current sheets. Observing the small-scale layers, typically referred to as diffusion regions [3–6], where kinetic effects are essential is a main goal of NASA’s MMS mission [7]. In the first phase of its mission, MMS collected high-resolution observations of electron diffusion regions near Earth’s magnetopause, where reconnection allows solar wind plasma to couple to and enter the Earth’s magnetosphere [8–14]. Reconnection at the magnetopause is characterized by strong asymmetries in the plasma and magnetic field conditions on either side [15–19], with the magnetosheath side containing high-density shocked solar wind plasma and the opposite magnetospheric side having a stronger magnetic field and hotter, more tenuous plasma. Depending on the orientation of the solar wind magnetic field, magnetopause reconnection may also occur with a variety of guide magnetic fields that reduce the total magnetic shear across the magnetopause current layer.

Fully kinetic simulations have been instrumental in understanding the details of the reconnection process in the complicated asymmetric geometry typical of the magnetopause, and the simulations have guided the interpretation of the data collected by spacecraft. So far, the vast majority of the simulations have been performed in 2D geometries, which have nonetheless captured many of the key field and particle signatures that have been observed in MMS data of magnetopause reconnection [20–28].

Two-dimensional simulations, however, preclude the development of an important class of instabilities. Of particular importance at the magnetopause are drift instabilities driven by the diamagnetic current carried by either electrons or ions at the steep density gradient between the magnetospheric and magnetosheath plasmas. The fastest growing modes of the lower-hybrid drift instability (LHDI) are approximately electrostatic [29], with typical wavelengths of order $k\rho_e \sim 1$ and frequencies of $\omega \sim \omega_{LH} = \omega_{pi}/\sqrt{(1 + \omega_{pe}^2/\omega_{ce}^2)}$ [30]. The mode is expected to be unstable under typical magnetospheric plasma conditions and has indeed been observed near magnetopause reconnection sites [31, 32] and in laboratory reconnection experiments [33–35].

Researchers have long speculated that LHDI fluctuations may contribute to anomalous

transport at the magnetopause. Lower-hybrid range fluctuations have been found to have electric potentials of amplitude $e\delta\phi/T_e \sim 0.1$ at both the magnetopause [36] and in the geomagnetic tail [37], suggesting that they could strongly interact with the electrons. This wave-particle interaction can lead to anomalous cross-field particle transport [29] that carries magnetosheath plasma into the magnetosphere even in the absence of magnetic reconnection [38, 39], and this particle mixing was observed in 3D kinetic simulation with weak guide field[40].

Important for reconnection, which requires a breaking of the electron frozen-in condition, the lower-hybrid fluctuations may also couple electrons and ions to produce an anomalous resistivity [41]. Because LHDI is weakened at higher plasma β (ratio of thermal pressure to magnetic pressure) [42] and takes on a longer wavelength electromagnetic character in the center of thin current sheets [30], it was not expected to contribute anomalous resistivity at the X-line during reconnection (where the in-plane magnetic field has a null). Indeed, in 3D simulations of reconnection with density asymmetries [43], the electrostatic LHDI was found to be localized to the density gradient region away from the X-line. More recent simulations [40, 44, 45], however, with very strong density and temperature asymmetries matching an MMS event with weak guide field [25], found that the electrostatic drift fluctuations could transiently penetrate into the X-line region. In addition, slower-growing electromagnetic fluctuations may persist and contribute to dissipation through a so-called anomalous viscosity [44, 46].

We re-examine the importance of drift fluctuations for anomalous transport and dissipation near magnetopause reconnection sites with a set of fully kinetic 3D simulations that match parameters from three MMS diffusion region encounters with varying guide magnetic fields [25, 26, 47]. The paper is outlined as follows: In Section II, we present the parameters and set-up of our fully kinetic particle-in-cell calculations. The cross-field particle transport and enhanced parallel electron heating induced by lower-hybrid range fluctuations are analyzed in Section III. We consider three different methods of quantifying the anomalous dissipation in the 3D simulations in Section IV, and a summary discussion follows.

II. PIC SIMULATIONS

We performed three 3D PIC simulations of reconnecting asymmetric current sheets using the code fully kinetic particle-in-cell code VPIC [48]. In order to use parameters relevant to Earth's magnetopause, the upstream plasma conditions on each side of the asymmetric current sheet were selected to match magnetopause conditions from three MMS diffusion region encounters with guide magnetic fields of ~ 0.1 [25] (some results from this run appear in [40]), ~ 0.4 [47], and ~ 1 [26] of the sheath reconnecting magnetic field component. While velocity shear across the magnetopause is common [49], we do not include bulk flows in our initial conditions. For each simulation, the computational domain is $L_x \times L_y \times L_z = 4096 \times 1024 \times 2048$ cells $= 40d_i \times 10d_i \times 20d_i$ (with d_i based on the initial sheath density). Macroparticles from the high-density sheath side and the low-density magnetosphere side are loaded as separate populations with different numerical macroparticle weights. This also allows us to quantify the mixing of particles originating from opposite sides of the magnetopause. In addition, the weights are selected so that the low-density magnetosphere plasma and the higher-density sheath plasma are each resolved with ~ 150 particles per species per cell, yielding $\sim 2.6 \times 10^{12}$ total numerical particles. For asymmetric layers with a larger density jump (up to a factor of ~ 16 in this paper), this approach is crucial for limiting the numerical noise.

The initial conditions include a Harris sheet current-carrying population superposed on an asymmetric Maxwellian background [43]. In particular, the initial magnetic field has components

$$\begin{aligned} B_x &= \frac{1}{2} \times \left[(B_1 - B_0) + (B_1 + B_0) \tanh\left(\frac{z}{\lambda}\right) \right] \\ B_y &= B_g \\ B_z &= 0 \end{aligned} \tag{1}$$

where we use subscript 0 to refer to upstream magnetosheath quantities and subscript 1 to refer to upstream magnetosphere quantities and the initial current sheet width is chosen as $\lambda = 1d_i$ (d_i is the ion inertial length based on the initial sheath density). Each background species (electrons and ions) is loaded as a Maxwellian with the following asymmetric temperature profile:

$$T_s = \frac{1}{2} \times \left[(T_{s1} + T_{s0}) + (T_{s1} - T_{s0}) \tanh\left(\frac{z}{\lambda}\right) \right]$$

TABLE I: Physics parameters used for VPIC simulations. The values are used to match conditions of the diffusion regions encountered by MMS in the references of the last column.

Run	B_g/B_0	β_0	n_1/n_0	B_1/B_0	T_{i0}/T_{e0}	T_{i1}/T_{i0}	T_{e1}/T_{e0}	$\omega_{pe0}/\omega_{ce0}$	Ref.
A	0.099	3.0	0.062	1.7	11	6.3	3.3	1.5	[25]
B	0.41	1.3	0.15	1.3	11	3.2	3.8	1.5	[47]
C	1.0	6.2	0.18	2.0	8.3	3.0	1.7	2.0	[26]

The total plasma density profile is then selected to establish gross single-fluid hydrodynamic pressure balance:

$$n = \frac{(p_1 + p_0) + (p_1 - p_0) \tanh(\frac{z}{\lambda})}{(T_1 + T_0) + (T_1 - T_0) \tanh(\frac{z}{\lambda})} + n_H \operatorname{sech}^2(z/\lambda) \quad (2)$$

where the total temperature $T_k = T_{ek} + T_{ik}$ and total pressure $p_k = n_k(T_{ek} + T_{ik})$ for $k = 0, 1$; the Harris density is $n_H = \mu_0(B_0 + B_1)^2/8T_H$; and we choose the Harris population temperature of each species $s = i, e$ to equal the hotter magnetospheric temperature: $T_{sH} = T_{s1}$. While the initial conditions are not an exact Vlasov equilibrium, the system rapidly settles into a quasi-equilibrium within a few ion gyroperiods [18, 43], which includes the development of a strong electrostatic field normal to the current sheet that confines the sheath ions and generates a strong electron $E \times B$ flow [18, 45]. Reconnection is seeded with a magnetic perturbation that generates a single X-line at the center of the current sheet extended in the y -direction. The reconnection rate typically peaks by a time of $t \sim 20/\omega_{ci}$. Unless otherwise noted, we plot data from times in the interval $t \sim (30-35)/\omega_{ci}$ during a period of quasi-steady reconnection. In Figs. 1(a-c), we plot the fully evolved current density from each 3D PIC simulation.

The fluctuations along the boundary layer separating the magnetospheric plasma from the reconnection exhaust have been identified as LHDI in previous work. They have a frequency near the lower-hybrid frequency and wave vectors with $\mathbf{k} \cdot \mathbf{B} \sim 0$ and $k\rho_e \sim 1$ [40, 44, 45]. In Run A with a weak guide field, there is also a large-scale kink of the current sheet with the lowest mode number that fits in the simulation domain. This is likely the electromagnetic branch of LHDI with $k\sqrt{\rho_e\rho_i} \sim 1$. It is stabilized by a guide magnetic field, and any kinking of the current sheet in Runs B and C is substantially weaker.

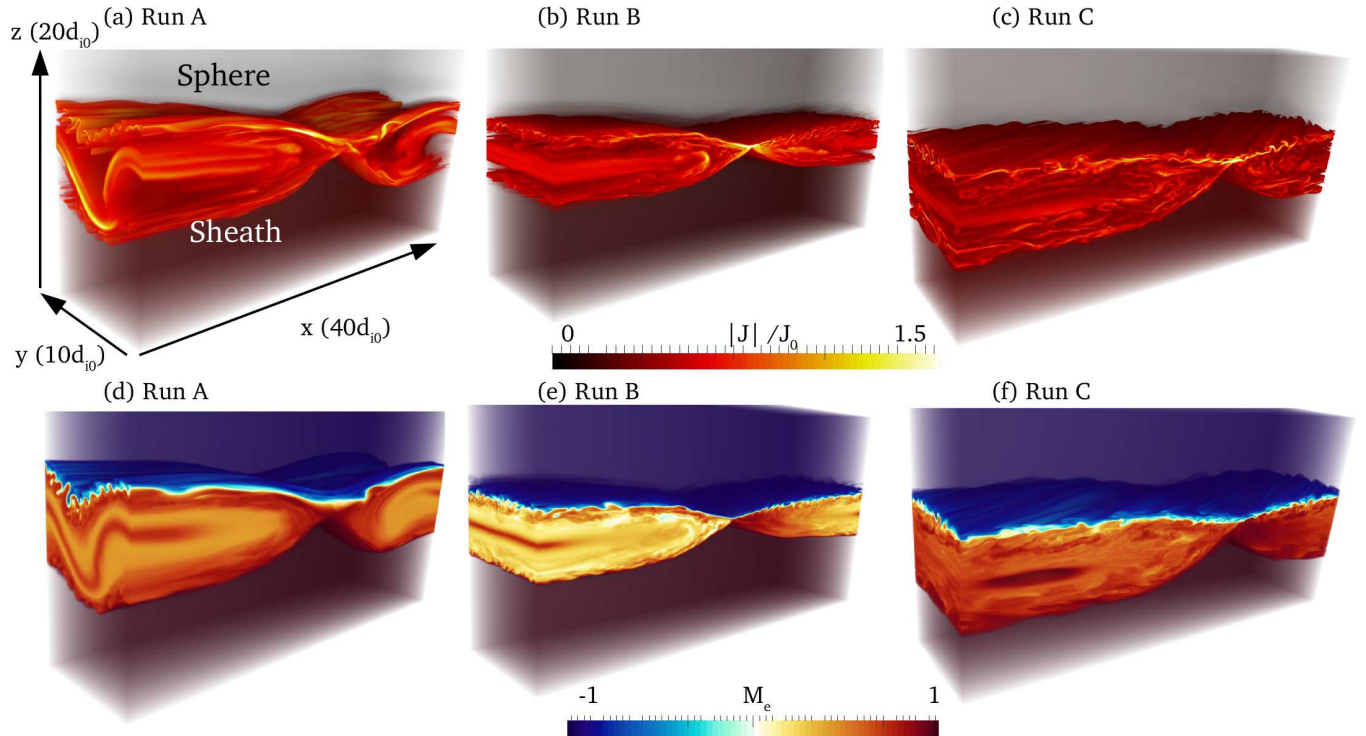


FIG. 1: Volume rendering of current density and electron mixing M_e from each 3D simulation. Each run here is shown at $t = 30/\omega_{ci}$.

III. PARTICLE TRANSPORT AND HEATING

As noted in the Introduction, the anomalous transport produced by LHDI across step density gradients was considered as a possible mechanism for regulating the thickness of Earth's magnetopause boundary layer [38, 39]. Even in the absence of magnetic reconnection, drift fluctuations may transport plasma from the dense magnetosheath across the magnetic field into the relatively tenuous magnetosphere. Here, we study the particle mixing of magnetosheath and magnetosphere plasma in our 3D kinetic simulations. The particles on opposite sides of the initial magnetopause current sheet are tagged separately, allowing their mixing over time to be diagnosed. We use the mixing measure introduced in Ref. [50] defined as:

$$M_e = \frac{n_{sh} - n_{sp}}{n_{sh} + n_{sp}} \quad (3)$$

where n_{sh} is the local number density of electron that originated in the magnetosheath and n_{sp} is the density of magnetosphere electrons. The mixing measure M_e varies from 1 where all electrons originate in the magnetosheath to -1 where all electrons are from the

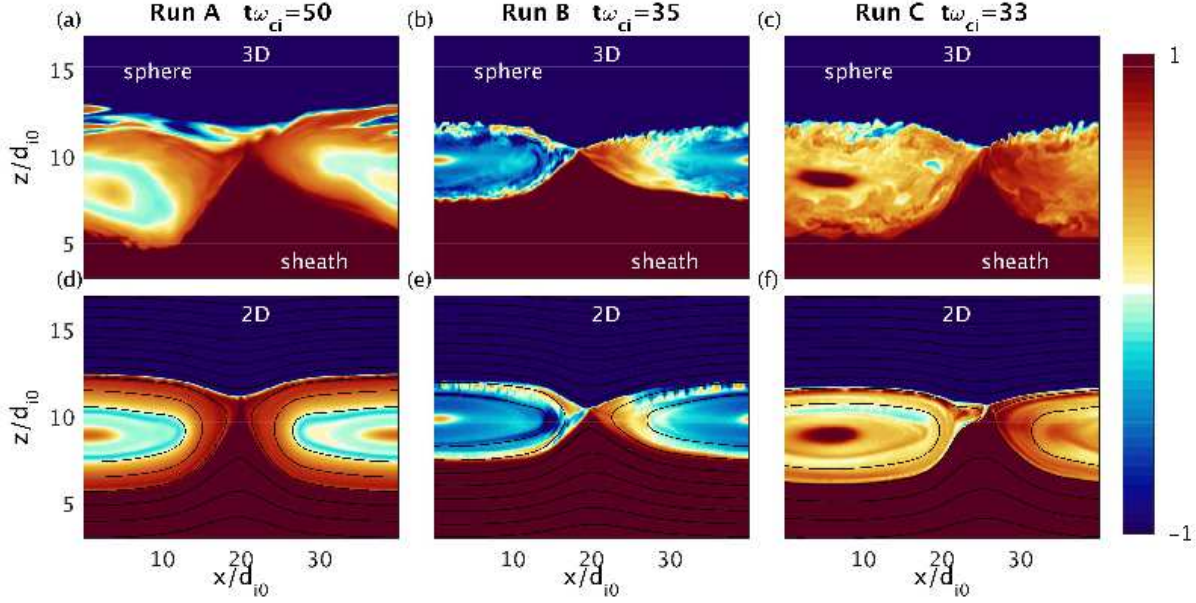


FIG. 2: M_e . Comparison of electron mixing diagnostic M_e introduced in Ref. [50] in each 2D and 3D simulation. Simulations are shown here are the last available time for each run.

magnetosphere. A 3D volume rendering of the mixing measure M_e from each 3D simulation is plotted in Figs. 1(d-f). The electron populations are strongly mixed within the region of LHDI fluctuations along the magnetospheric separatrix.

In Fig. 2, M_e is plotted from each 3D simulation in the top panels and from a corresponding 2D simulation in the lower panels. For the 2D simulations in Figs. 2(d-f), sample in-plane magnetic field lines, which are contours of the out-of-plane magnetic vector potential A_y are also indicated. Note that because the canonical momentum $p_y = mv_y - eA_y$ is strictly conserved in 2D, each electron never moves farther than an in-plane Larmor radius from a single magnetic flux surface. The particle mixing is therefore limited to an electron orbit width across the magnetic separatrices [22], resulting in the sharp boundaries in M_e across the magnetopause surface. In a system with 3D fluctuations, however, no conservation property prohibits electrons from being transported across the magnetic separatrices [40]. In fact, in Figs. 2(a-c), there is a region of strong magnetosheath and magnetosphere mixing particularly along the magnetospheric separatrix where the density gradient and LHDI fluctuations are strongest. There is evidence of the electron mixing in MMS observations of magnetopause reconnection sites. In particular, a population of lower-energy electrons presumed to be sourced from the magnetosheath have been observed in the magnetosphere

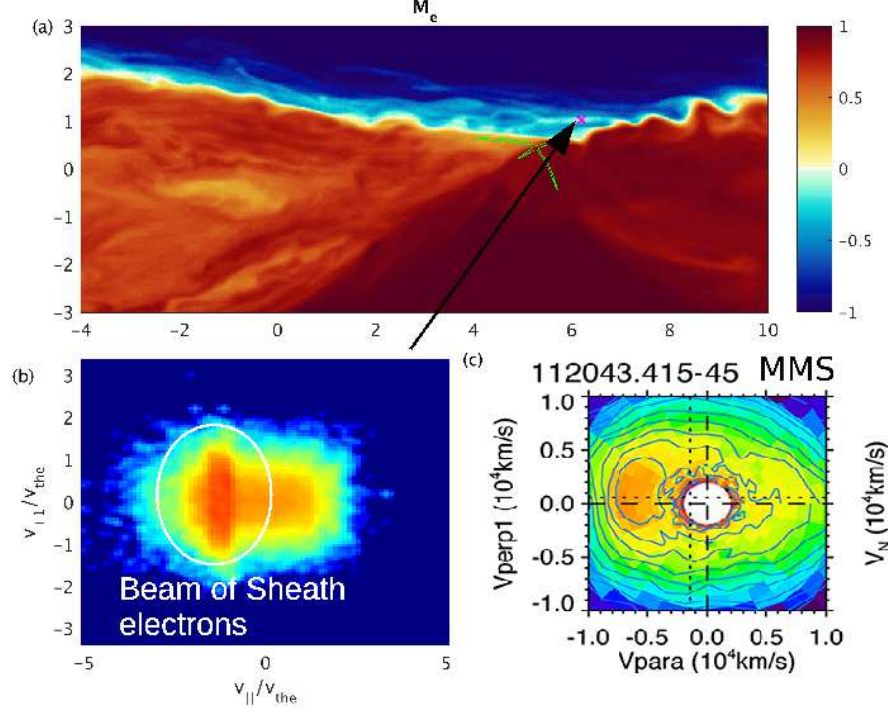


FIG. 3: (a) Mix measure M_e near the approximate X-line (indicated by green contours) in Run C with $B_g/B_0 \sim 1$. (b) An electron distribution in $v_{\parallel} - v_{\perp}$ space at the point marked \times in panel (a), which exhibits a parallel beam of sheath electrons. (c) A similar electron distribution from MMS observations [26] of a magnetopause reconnection event with parameters matching this simulation.

inflow region in conjunction with LHDI fluctuations at the current density layer [32]. In addition, beams of electrons, presumed to be sourced from the magnetosheath, have been observed in the magnetospheric inflow. An example of a parallel beam of magnetosheath electrons (identified by their particle tag in the simulation) is plotted in Fig. 3(b) from the point labeled \times in Fig. 3(a). In this particular distribution, the sheath electron beam is moving towards the X-line ($v_{\parallel} < 0$), although distributions from nearby regions display sheath beams moving away from the X-line. A similar distribution measured by MMS [See Fig. 8 of Ref. [26]] is plotted in Fig. 3(c) from the event with parameters matching this simulation, where the parallel beam of high phase-space density is presumed to be composed of electrons that originated in the sheath.

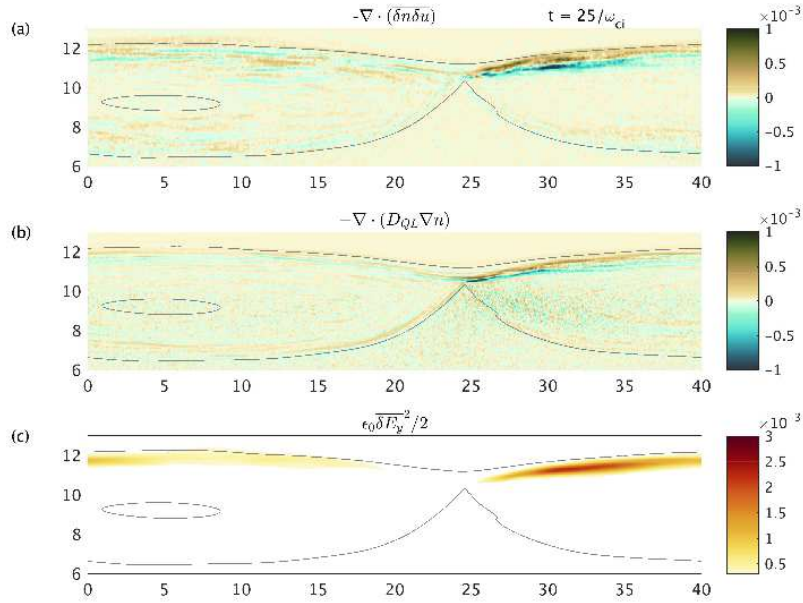


FIG. 4: (a) Fluctuating particle transport across the magnetospheric separatrix in Run C ($B_g/B_0 \sim 1$) at $t = 25/\omega_{ci}$. (b) Quasi-linear estimate for the particle transport induced by LHDI. (c) The fluctuation amplitude of the electric field directly evaluated from the simulation data. Gray lines mark where the electron mix measure $M_e = \pm 0.9$.

A. Quasi-Linear Estimates

The enhanced particle mixing observed in 3D was is a direct result of out-of-plane fluctuations. As a first method to quantify the anomalous or fluctuation-induced particle transport across the magnetospheric separatrix, we employ spatial averaging in the y direction [40, 43, 44, 46, 51]. We split each quantity Q into mean and fluctuating components defined as $Q = \overline{Q} + \delta Q$, with the mean component given by the y -average over the simulation domain:

$$\overline{Q}(x, z, t) = \frac{1}{L_y} \int_0^{L_y} Q(x, y, z, t) dy, \quad (4)$$

and where the fluctuating component satisfies $\overline{\delta Q} = 0$ by construction. Note that for pairs of quantities Q and R , $\overline{QR} = (\overline{Q})(\overline{R}) + \overline{\delta Q \delta R}$, and the anomalous particle transport is ascribed to the correlated fluctuations in density and bulk flow, $\overline{\delta n \delta \mathbf{u}}$.

In the quasi-linear approximation, the fluctuating density δn and electron drift $\delta \mathbf{u}$ are computed for LHDI from linear instability theory, and the net particle flux $\overline{\delta n \delta \mathbf{u}}$. The

density profile is then predicted to relax through a diffusion equation of the form $\partial\bar{n}/\partial t \sim \nabla \cdot (D_{QL}\nabla\bar{n})$, where the anomalous particle flux $\overline{\delta n\delta\mathbf{u}}$ is proportional to the gradient of the mean density profile $\nabla\bar{n}$ through a diffusion coefficient D_{QL} . For LHDI, the quasi-linear diffusion coefficient D_{QL} is given by [38, 52]

$$D_{QL} \sim 0.5\rho_e^2\nu_{QL}\left(1 + \frac{T_i}{T_e}\right) \quad (5)$$

where the effective anomalous collision frequency is

$$\nu_{QL} \sim 0.6\omega_{lh} \left(1 + \frac{\omega_{pe}^2}{\omega_{ce}^2}\right) \frac{m_i}{m_e} \frac{E_f}{nT_i} \quad (6)$$

and $E_f \sim \epsilon_0(\overline{\delta E_y})^2/2$ is the energy density of the fluctuating electric field. The energy density of the fluctuating electric field E_f in the saturated state is estimated to be [53]

$$E_f \sim \frac{nm_e V_d^2}{4(1 + \omega_{pe}^2/\omega_{ce}^2)} \quad (7)$$

given in terms of the relative drift velocity V_d between the electrons and the ions. This estimate agrees with the peak fluctuation amplitudes in the simulations within a factor of order unity. The spatial dependence of the fluctuation amplitude, however, depends also on the details of the drift velocity, magnetic field, and density profiles. In order to compare the quasi-linear estimate to the simulations, we evaluate the average fluctuation amplitude $\overline{\delta E^2}$ directly from the simulation [see Fig. 4(c)]. An example from Run C with $B_g/B_0 \sim 1$ is plotted in Figures 4(a-b), and we find good agreement between the fluctuating particle flux and the quasi-linear theoretical estimate.

The coefficient D_{QL} has been estimated directly from observations by time-filtering multi-spacecraft measurements of the ratio $\overline{\delta n\delta\mathbf{u}}/\nabla\bar{n}$ [31], and it was found to agree with theoretical predictions. In MMS observations of a magnetopause reconnection event [32], a peak value of $D_{QL} \sim 0.8 \times 10^9$ m/s² was found. Based on a typical fluctuating electric field of $|\delta E| \sim 20$ mV/m for the same event, we find $D_{QL} \sim 0.6 \times 10^9$ m/s² following on Eq. 6. Taking an average drift velocity $V_d \sim 300$ km/s yields $D_{QL} \sim 0.1 \times 10^9$ m/s² using Eq. 7, which is also in rough agreement with the observed values, though smaller than the peak value.

Because of the signs of the terms in Figs.4(a-b), the main effect of the turbulent transport is to relax the density gradient across the magnetospheric separatrix. This process thus carries plasma from the high density magnetosheath plasma into the magnetospheric inflow

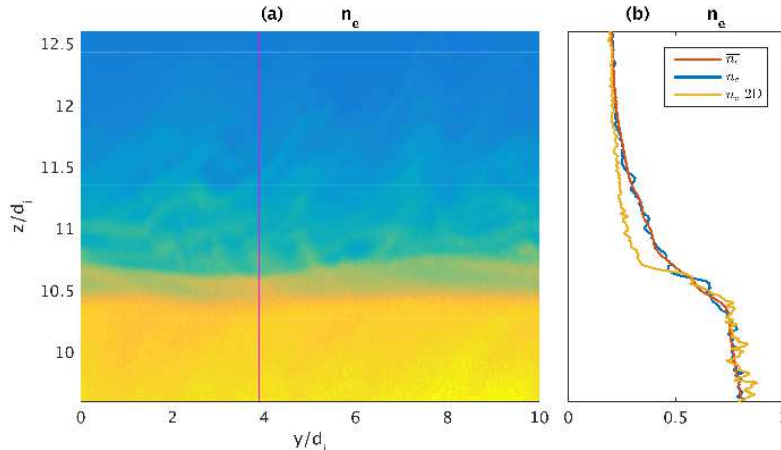


FIG. 5: (a) Cut at the X-line of the electron density in the $y - z$ plane from Run C ($B_g/B_0 \sim 1$) at $t\omega_{ci} = 30$. (b) Line out of the density profile across the current sheet along the cut indicated in (a) along with corresponding cuts of the y -averaged density profile, and the density profile from a 2D simulation. Particle transport across the magnetospheric separatrix relaxes the density gradient.

region. Figure 5 compares the 3D density profile across the current sheet to the y -averaged and the 2D density profiles. In agreement with Ref. [45], the 3D density profile is broadened compared to 2D.

B. Magnetic Field Line Mixing vs. Cross-field Transport

Within the quasi-linear theory of transport by electrostatic LHDI, the fluctuating electron drift results from $\mathbf{E} \times \mathbf{B}$ motions across the magnetic field. The magnetosheath electrons within the turbulent mix layer along the magnetospheric separatrix are mixed by cross-field transport, rather than by parallel streaming along mixed magnetic field lines. To verify this, we study the magnetic geometry and topology.

In guide field regime (without magnetic nulls), well-defined topological boundaries between reconnected magnetic field domains may not exist. In this limit, the concept of quasi-separatrix layers (QSLs) was introduced to identify regions where the magnetic field lines very rapidly diverge [54, 55], which coincide with topological separatrices when applied to 2D systems. The QSLs may be calculated with the so-called squashing factor [55], a geometric measure computed from the map that takes initial seed points to final points a finite distance away along the magnetic field. To locate an approximate QSL in our runs,

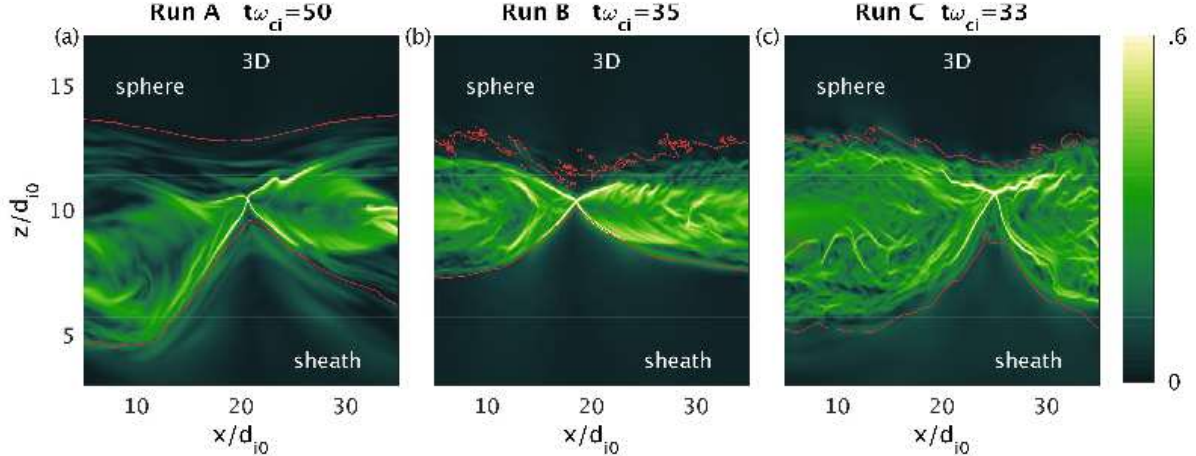


FIG. 6: The magnetic field exponentiation factor σ [50] from a plane of seed points in each 3D simulation. Plotted here is $\max(\sigma_b, \sigma_f)$, where each σ is calculated by tracing either *forward* or *backward* along the magnetic field lines. The ridges of large values highlight the quasi-separatrix layer (QSL), which is an approximate X-line and pair of separatrices. The red contour in each panel marks where the electron mix measure $M_e = 0.99$.

we compute a closely related measure, the exponentiation factor σ [50, 56], which is also calculated by finding magnetic field lines. We trace magnetic field lines a distance of $L = 5d_{i0}$ in the forward (along \mathbf{B}) and backward (along $-\mathbf{B}$) directions from each point \mathbf{x}_0 within a seed plane to some final point \mathbf{x}_f . The factor σ is then defined as $\sigma = \log \sqrt{\lambda_m}$, where λ_m is the maximal eigenvalue of the symmetric matrix

$$\left(\frac{\partial \mathbf{x}_f}{\partial \mathbf{x}_0} \right)^T \left(\frac{\partial \mathbf{x}_f}{\partial \mathbf{x}_0} \right). \quad (8)$$

The QSL may be visualized as the region of large values of σ . In Fig. 6, we plot the maximum of the forward and backward σ values. In each case, a ridge of large values is found near the approximate X-line, highlighting the QSLs within the reconnection region branching out from the approximate X-line.

Also plotted in Fig. 6 are contours where the electron mix measure $|M_e| = 0.99$, meaning that beyond these boundaries there is practically no mixing of magnetosheath and magnetosphere electrons. Particularly on the magnetosphere side at weaker guide fields, the electron mixing contour is separated from the QSL, confirming that there is relatively little mixing of magnetic field lines although there is particle mixing. This is as opposed to previous 3D simulations of asymmetric reconnection [50], where the electron mixing was mainly at-

tributed to parallel streaming along reconnected field lines, and the electron mixing contour was a good proxy for the magnetic separatrix, as demonstrated by field line tracing.

In the absence of strong cross-field electron transport, the reconnection rate may be computed by calculating the change in flux of the reconnecting magnetic field in the region of no electron mixing [50]. We apply this diagnostic to our runs, and the results are plotted in Fig. 7, where the rates are normalized using a hybrid magnetic field and Alfvén speed based on values on both sides of the asymmetric layer following the conventions of Ref. [15]. As expected, the diagnostic is not suitable near the magnetosphere separatrix, where fluctuation-induced particle transport carries magnetosheath electrons across the magnetic separatrix. On the magnetosheath side, however, cross-field electron transport is weak, and we expect the diagnostic to give a good estimate of the global reconnection rate. In fact, the global reconnection rates measured in this way are nearly identical in 2D and on the magnetosheath side in 3D, with normalized rates of ~ 0.05 [57]. This suggests that while the strong turbulence that develops along the magnetosphere separatrix affects plasma transport across the magnetopause, it ultimately has little effect on the overall rate of reconnection.

C. Enhanced Parallel Heating

For the weak guide field case, it was previously demonstrated that the particle mixing region also exhibits enhanced heating of the electrons in the direction parallel to the magnetic field [40]. In Fig. 8, the parallel electron temperature $T_{e\parallel}$ is plotted from each of the three 3D simulations. In all three cases, similar enhancement of $T_{e\parallel}$ is observed within the fluctuation mix layer. In Ref. [40], the locally sourced electrons in the inflow regions were found to obey relatively simple equations of state [58–60] that resemble the CGL [61] scalings $T_{e\parallel} \propto n^2/B^2$ and $T_{e\perp} \propto B$. The increase of temperature with density implied that the heating was essentially caused by an adiabatic compression of the electron fluid. The simple scaling, however, only applied to electron populations in each inflow region that had remained on a given side of the separatrix, not those that mixed from the opposite side..

A survey of MMS observations of magnetopause reconnection sites found that in most cases a region exists in the magnetospheric inflow where the electron parallel temperature falls even while the density increases [62]. Because this region was found to cover length scales larger than the electron Larmor radius, the discrepancy with the fluid equations of

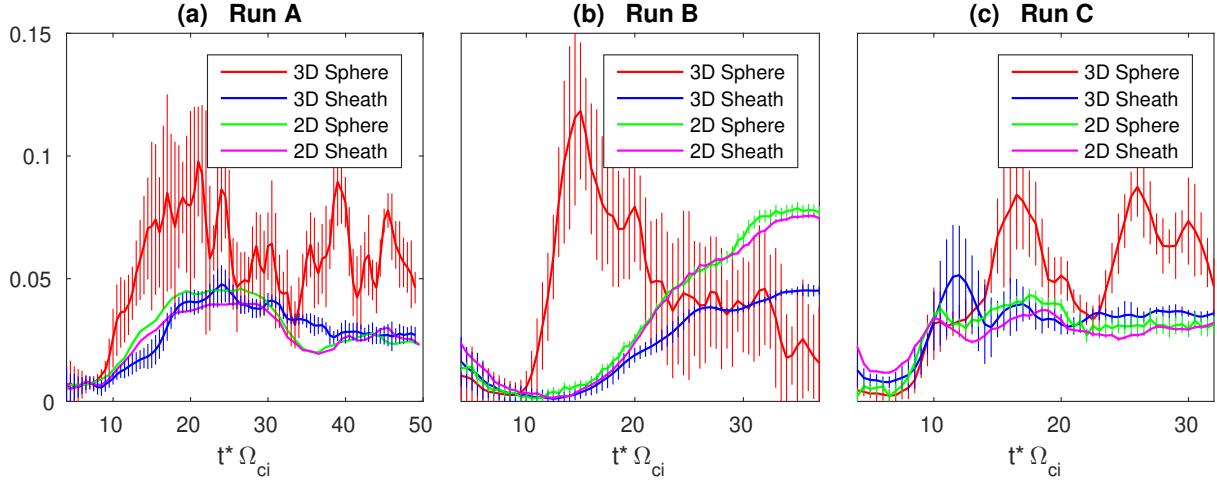


FIG. 7: Comparison of inferred reconnection rates over the course of each 2D and 3D simulation evaluated with the electron mixing diagnostic introduced in Ref. [50]. The method cannot be used to determine a magnetic reconnection rate on the magnetospheric side because turbulence transports electrons across the magnetospheric separatrix. On the sheath side, however, there is little cross-field particle transport, and the rate is similar in 2D and 3D simulations (except that Run B developed a large secondary island in 3D at $t \sim 20/\omega_{ci}$ that reduced the global rate). The 3D fluctuations do not strongly modify the overall reconnection rate. The "error bars" are the variance of the rate measure over a set of cuts at different x values along the length of the current sheet (see Appendix of [50] for detailed explanation).

state predictions was attributed to anomalous particle mixing. We confirm that these signatures are present in our 3D simulations. Figure 9(a) shows the parallel electron temperature $T_{e\parallel}$ in Run C with a strong guide field. Sample in-plane projections of 3D magnetic field lines are plotted in blue. The bottom blue line is approximately within the separatrix layer and delineates the magnetospheric inflow from the reconnection exhaust. The density and parallel temperature profiles across the current sheet are plotted in Fig. 9(b) [along the cut marked in green in Fig. 9(a)]. As observed in the MMS data survey, $T_{e\parallel}$ drops within the inflow region even as the total electron density continues to increase. This occurs several times farther from the magnetic separatrix than the electron Larmor radius ρ_e , plotted Fig. 9(b). This indicates that the mixing results not only from finite electron orbit effects, which are limited to ρ_e length scales and also occur in 2D [5, 22, 27]. To demonstrate that this region indeed contains magnetosheath electrons mixed into the magnetosphere inflow, reduced

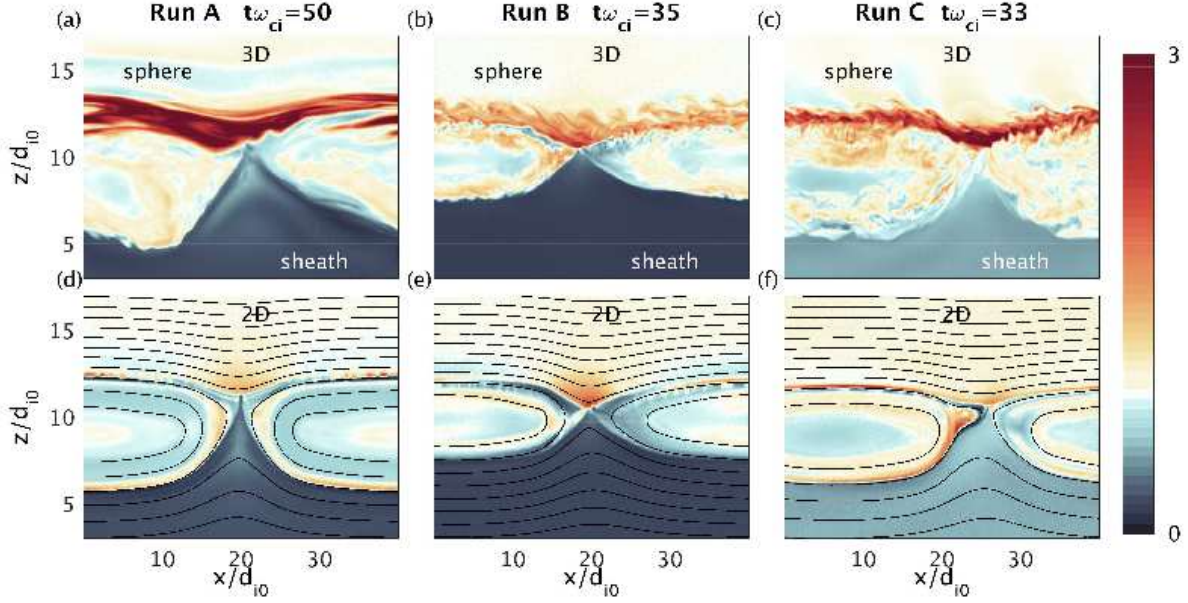


FIG. 8: Comparison of parallel electron temperature in each 2D and 3D simulation. Note the enhanced $T_{e\parallel}$ within the mix layer near the magnetospheric separatrix in each 3D simulation.

electron velocity distributions in the $v_{\parallel} - v_{\perp}$ (directions with respect to local magnetic field) are plotted in Fig.9(c). Because the numerical particles are tagged as originating on the magnetosphere or magnetosheath sides of the simulation, we are able to generate separate plots for the sheath and sphere electrons. At point *I* [marked in Figs.9(a-b)] roughly $4\rho_e$ into the magnetosphere inflow, a large population of relatively low-energy sheath electrons is present. These electrons account for the increased density and the lower electron temperature. The sheath population becomes smaller deeper into the magnetosphere inflow, as seen for points *II* and *III*.

IV. OHM'S LAW AND MEASURING ANOMALOUS RESISTIVITY

The anomalous particle transport induced by lower-hybrid fluctuations is associated with a corresponding anomalous resistivity [29]. Historically, there was strong interest in anomalous resistivity because observed reconnection rates are far faster than Sweet-Parker estimates in a plasma with classical resistivity [63]. It was proposed, for example, that LHDI could generate anomalous resistivity and enhance reconnection rates in Earth's geomagnetic tail [41]. Indeed, for plasma and magnetic field parameters typical of magnetospheric recon-

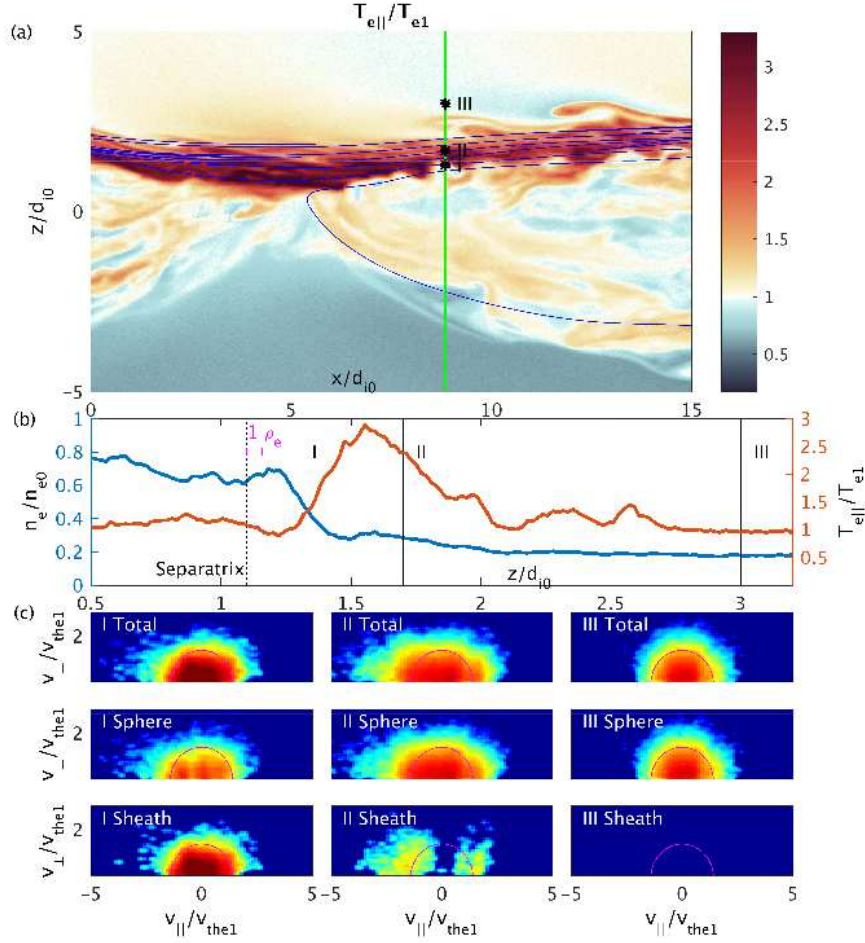


FIG. 9: (a) Parallel electron temperature from Run C with order unity guide field. The blue contours are in-plane projections of magnetic field lines. (b) Line outs of the density and parallel electron temperature along the z cut marked in green in (a). The location of the last un-reconnected magnetospheric field line is marked by the dashed line. (c) Reduced electron velocity distribution functions in v_{\parallel} - v_{\perp} space from the points labeled *I*, *II*, and *III* in (a-b). The top row shows the total electron distribution, the middle row shows only particles that originated on the magnetosphere side, and the bottom row includes only electrons from the magnetosheath. Circular magenta contours are for reference to aid in seeing anisotropy.

nection sites, order of magnitude estimates suggest that anomalous resistivity from lower-hybrid range fluctuations could be important for breaking the frozen-in condition near the X-line [64]. It has become clear, however, that reconnection can be fast in thin current

sheets when kinetic or multi-fluid effects are taken into account [65–71]. In collisionless space plasmas, laminar inertia and pressure tensor terms from 2D models [5, 6] are sufficient to yield the observed fast reconnection rates. Of course, in naturally formed 3D systems, anomalous dissipation may still be produced. To be a dominant factor in governing the reconnection rate, however, the anomalous dissipation would have to significantly broaden the electron layer to reduce the laminar kinetic contributions.

Quantifying the importance of the anomalous contributions compared to essentially 2D kinetic effects has proven challenging. For example, the simple theoretical estimates rely on a number of approximations, notably assuming purely electrostatic fluctuations in a uniform equilibrium. Near the X-line of reconnecting current sheets, electromagnetic instabilities or corrections for high plasma β [30, 42, 72–74] and stabilization by magnetic shear [75] should be taken into account. Furthermore, the growth of any given instability must compete with the fast convection time for a fluid element transiting the diffusion region [43]. Because of these and other complications, evaluating the contribution of kinetic instabilities within realistic reconnection geometries has relied heavily upon numerical simulations for both the linear [30] and the non-linear regimes [40, 43, 44, 46, 76–80]. Meanwhile, in laboratory reconnection experiments, lower hybrid range fluctuations were observed within reconnecting current sheets [33, 81, 82]. Both 3D kinetic modeling [83] and subsequent experiments [84] found that the fluctuations were too weak to substantially modify the reconnection physics..

A. Spatial y -Averaging

As a first method to attempt to quantify the turbulent or anomalous contributions to the reconnection electric field, we use y -averaging [40, 43, 44, 46, 51] as was used in Section III. We start with the electron momentum balance, or Ohm’s Law, equation,

$$ne(\mathbf{E} + \mathbf{u} \times \mathbf{B}) = m \left[\frac{\partial(n\mathbf{u})}{\partial t} + \nabla \cdot (n\mathbf{u}\mathbf{u}) \right] + \nabla \cdot \mathbb{P}_e, \quad (9)$$

where \mathbb{P}_e is the electron pressure tensor. Then the y -averaged momentum balance equation yields:

$$\overline{ne}(\overline{\mathbf{E}} + \overline{\mathbf{u}} \times \overline{\mathbf{B}}) = m \left(\frac{\partial(\overline{n\mathbf{u}})}{\partial t} + \nabla \cdot [(\overline{n\mathbf{u}})(\overline{\mathbf{u}})] \right) + \nabla \cdot \overline{\mathbb{P}_e} - e\overline{\delta n \delta \mathbf{E}} - e\overline{\delta(n\mathbf{u}) \times \delta \mathbf{B}} + m\nabla \cdot [\overline{\delta(n\mathbf{u})\delta \mathbf{u}}], \quad (10)$$

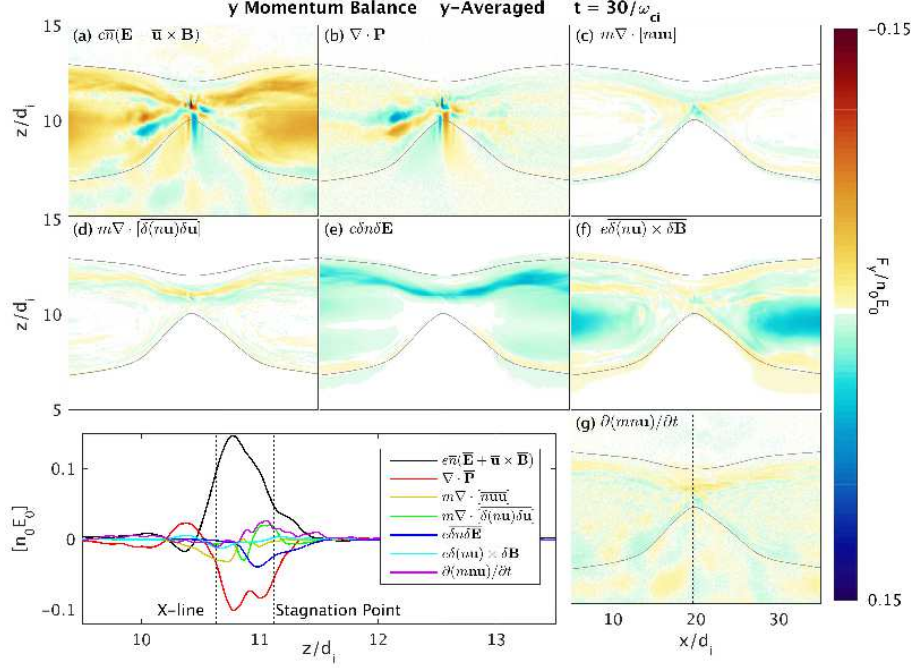


FIG. 10: Terms in the y-averaged Ohm's law contributing to electron momentum balance from Run A with weak guide field. Anomalous resistivity $\propto \overline{\delta n \delta \mathbf{E}}$ contributes appreciably to the non-ideal electric field near the stagnation point at the simulation time ($t = 30/\omega_{ci}$) shown. However, this is likely a transient effect since at later times the relative importance is diminished.

where we have chosen to retain the particle flux $n\mathbf{u}$ as a single quantity when decomposing products of terms. The anomalous terms are those that contain correlated fluctuations, and $\overline{\varepsilon \delta n \delta \mathbf{E}}$ is commonly referred to as an anomalous resistivity. The remaining two terms have been combined and called anomalous viscosity [44, 46]. To differentiate between them here, we will refer to $\overline{\varepsilon \delta(\overline{n \mathbf{u}}) \times \delta \mathbf{B}}$ as the anomalous Lorentz force and $m \nabla \cdot [\overline{\delta(\overline{n \mathbf{u}}) \delta \mathbf{u}}]$ as the Reynold's stress contribution.

The various contributions to the y-averaged out-of-plane electron momentum balance equation in a sample plane from each 3D simulations are plotted for Run A in Figs. 10(a-g), Run B in Figs. 11(a-g), Run C in Figs. 12(a-g). Panel (h) of each figure shows a line out of the terms along a cut through the X-line across the current sheet [indicated in each panel (g)]. In asymmetric reconnection, the X-line and the electron flow stagnation may be spatially separated [15]. For 2D systems without a guide field, the reconnection electric field in the region between the X-line and stagnation point was found to be supported by electron inertia (especially near X-line) and the divergence of the electron pressure tensor [5].

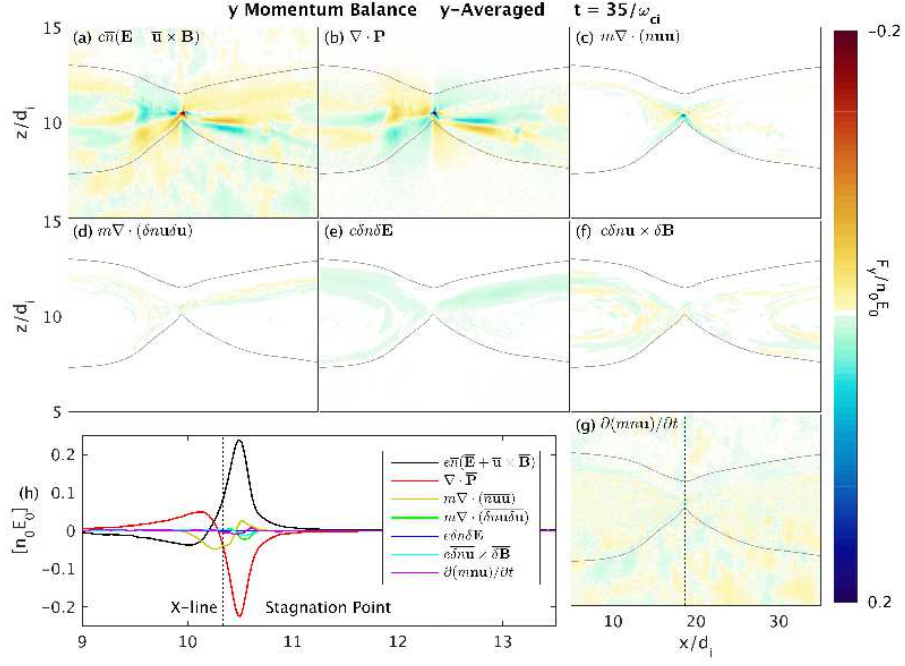


FIG. 11: Terms in the y-averaged Ohm's law contributing to electron momentum balance from Run B with $B_g/B_0 \sim 0.4$. The anomalous terms are negligible.

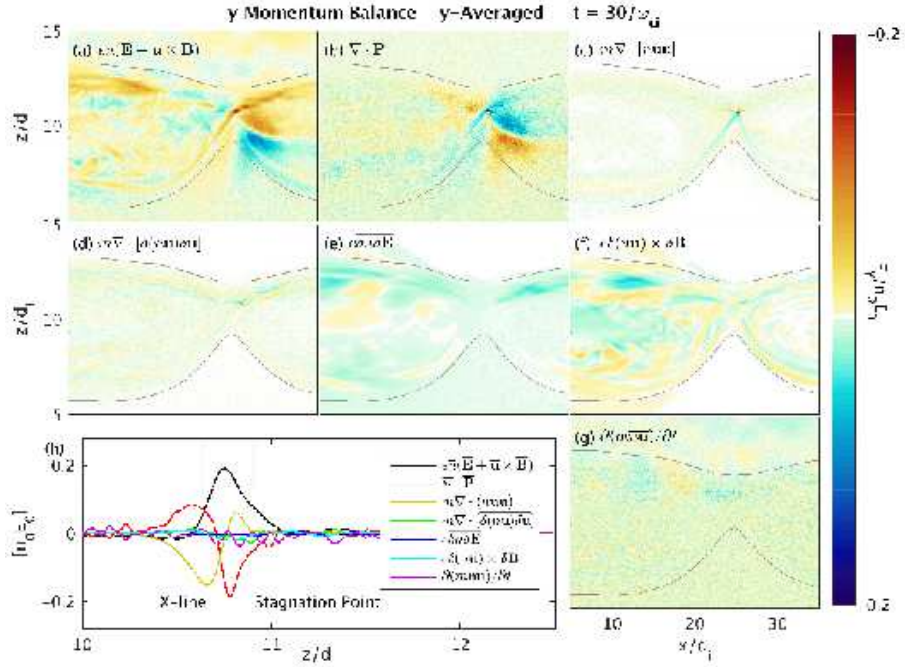


FIG. 12: Terms in the y-averaged Ohm's law contributing to electron momentum balance from Run C with order-unity guide field. The anomalous terms are negligible.

In Runs B and C with moderate and stronger guide fields, we find that the 2D-like inertial and pressure terms continue to dominate in the Ohm's law. The anomalous contributions are small throughout these simulations.

In Run A with a weak guide field, y -averaging does produce anomalous contributions to Ohm's Law. In Fig. 10(h), for example, it is seen that the anomalous resistivity $\propto \overline{\delta n \delta E_y}$ is as large as the electron inertia, particularly near the stagnation point. However, as noted earlier papers [40, 45], this anomalous resistivity is transient, and it subsides after the initial burst of LHDI becomes weaker. This implies that the observed anomalous resistivity is driven by the sharp gradients set up by the initial conditions containing a thin sheet and magnetic perturbation. Figure 13 shows the contributions to the y -averaged Ohm's Law at a later time of $t\omega_{ci} = 45$. In the cuts through the X-line in Fig. 13(h), the anomalous resistivity is negligible. On the other hand, the anomalous Lorentz $\propto \overline{\delta(n\mathbf{u}) \times \delta\mathbf{B}}$ term is large, and even dominant, over a broad region between the X-line and the stagnation point, in agreement with previous simulations [45]. We attribute this to the development of the electromagnetic LHDI [30] that results in a kinking of the current sheet over a longer time scales. Recall, however, that the overall reconnection rate is similar for this run in 2D and in 3D.

One complication of the y -averaged Ohm's Law is that its interpretation assumes that, on average, the system remains translationally invariant in the y -direction. The current sheet, however, may be unstable to a kink instability [most apparent in the weak guide field Run A in Fig. 1] with a wavelength several times larger than the electrostatic LHDI fluctuations. The observed wavelength of the kink instability observed in the present simulation ($k \sim 2\pi/L_y \sim 0.6/d_{i0}$) is consistent with the longer wavelength electromagnetic LHDI [79]. Even a moderate kinking of the current sheet entails variations in the y -direction. See, for example, Fig. 14(c), which shows a cut in the $y - z$ plane of the electron current density at the approximate X-line in Run C with a strong guide field. The strong guide field of Run C tends to stabilize kink instabilities, and the kinking is considerably weaker than in the low guide field case of Run A [Fig. 14(a)]. Even so, the small kink of the current sheet creates a broader current profile when the current density is y -averaged [see Fig. 14(b)]. Locally, however, the current density remains similarly peaked in 2D and 3D with a full width at half max of $\sim 2d_{e0}$ in each of the 3D runs, suggesting that the underlying dissipation physics is the same.

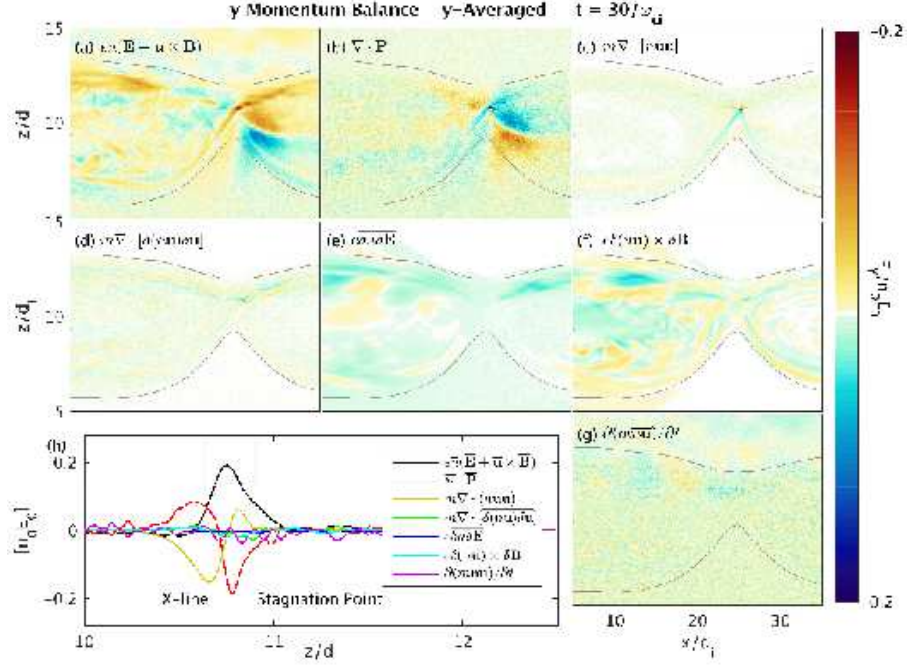


FIG. 13: Terms in the y -averaged Ohm's law contributing to electron momentum balance from Run A with weak guide field at late time in the simulation. At this stage of the simulation, the anomalous Lorentz force $\propto \overline{\delta(n\mathbf{u}) \times \delta\mathbf{B}}$ piece of the anomalous viscosity is large.

To highlight the effect of the longer wavelength kinking on the y -averaged Ohm's law, we plot cuts of the electron momentum balance equation in Fig. 15 where the y -average is taken over two different subsets of the domain of length $2.5d_{i0}$ (one quarter of the simulation). This range covers ~ 3 wavelengths of the electrostatic LHDI fluctuations, and so if the short wavelength waves contributed consistently to anomalous dissipation over the length of the simulation box, the contributions to the Ohm's law should be similar for the two cases. On the contrary, the first segment for $y \in [0, 2.5]d_{i0}$ [Fig. 15(a)] is from a region where the current is kinked and misaligned with the y direction [see Fig. 14(a)]. Here, there is a large contribution from the time derivative term. For $y \in [5, 7.5]d_{i0}$ [Fig. 15(a)] on the other hand, the phase of the kink leaves the current sheet locally nearly aligned with y -direction, and the Ohm's law looks essentially 2D, with very small contributions from anomalous or time-varying terms. This strongly suggests that the anomalous viscosity that appears in Fig. 13 is thus not caused by shorter wavelength contributions that add up consistently over the full length of the domain, but it is rather a result of the $m = 1$ longer wavelength kinking of the current sheet.

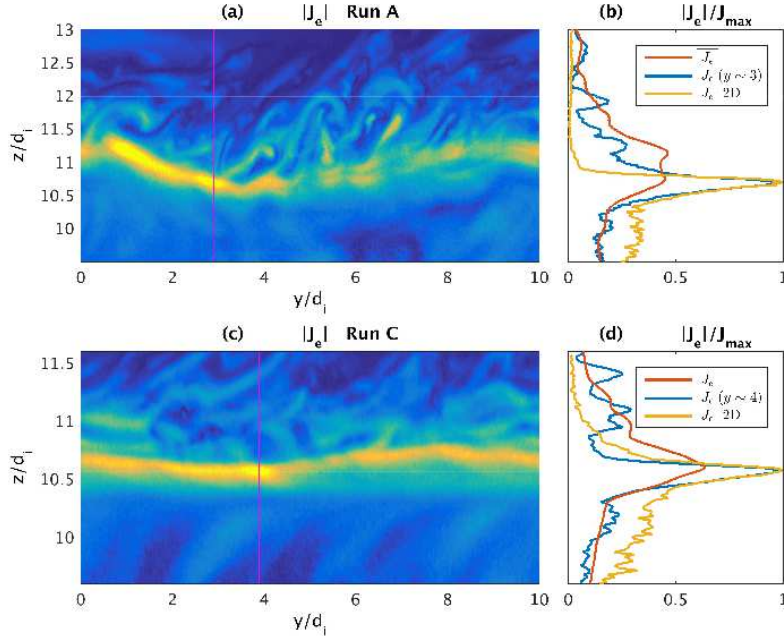


FIG. 14: The electron current density $|J_e|$ in the y (principal current flow direction) and z (normal to the current sheet) plane at the x location of the X-line from (a) Run A with weak guide field and (c) Run C with strong guide field. (b,d) Cuts through the normal z direction of the y -averaged current density $\overline{|J_e|}$, of the current density through the cuts indicated in (a,c), and from the corresponding 2D simulations. The current sheet width is locally similar in 2D and 3D, while the y -averaged profile appears broader because of the longer wavelength kink of the current layer.

B. Temporal t -Averaging

As an alternative to y -averaging, which can introduce spurious broadening of spatial profiles, we evaluate here time-averaging. We define the t -average of any quantity Q as

$$\tilde{Q}(x, y, z, t_0) = \frac{1}{\Delta t} \int_{t_0}^{t_0 + \Delta t} Q(x, y, z, t) dt \quad (11)$$

For Run C, we averaged over intervals of 200 numerical time steps, so that $\Delta t \sim 5.6/\omega_{ce0} \sim 0.65/\omega_{lh}$, where ω_{lh} is the lower hybrid frequency evaluated within the turbulent magnetospheric boundary layer. Unfortunately, for Run C the averaging interval therefore did not cover a full period of the lower hybrid fluctuations. Because of the large data storage requirements of these 3D simulations, the time-averaging must be performed in-line. Changing the time-averaging interval would thus require re-running the simulation, which is not presently feasible. For Run B, on the other hand, the time-averaging interval was set

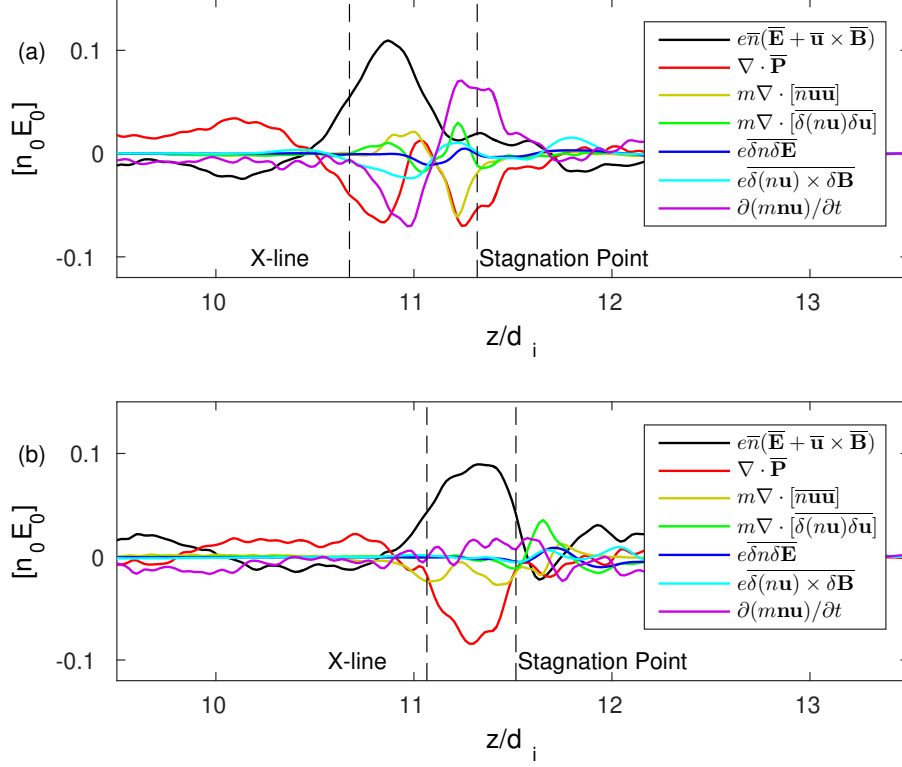


FIG. 15: Cuts across the current sheet through the X-line of the y -averaged Ohm's law from Run A at $t = 45/\omega_{ci}$, with the average taken over a subset of the simulation domain in the range (a) $y \in [0, 2.5]d_{i0}$ and (b) $y \in [5, 7.5]d_{i0}$. The anomalous terms are not consistent with averaging over the whole domain in Fig. 13(h), suggesting that they do not result from the short wavelength fluctuations.

to 2000 numerical total time steps with every tenth step included in the average. In this way, the averaging interval covered a full cycle of the lower-hybrid range fluctuations. (The time-averaging diagnostic was unavailable for Run A.)

The contributions to the t -averaged Ohm's Law from Run B are plotted in Fig. 16. The dashed gray curve marked "Total" is the sum of the contributions, and small deviations from zero indicate numerical noise. We find in this case that the Reynold's stress $\propto \nabla \cdot [m\delta(\widetilde{n\mathbf{u}})\delta\mathbf{u}]$ takes on values comparable to the reconnection electric field. The values oscillate, however, and they take opposite signs for different choices of the 2D $x - z$ plane in the simulation volume. The other contributions are similar to 2D, with inertia and the pressure tensor both contributing to the non-ideal electric field. In Fig. 17, the various contributions to the t -averaged Ohm's Law are plotted from Run C with $B_g/B_0 \sim 1$. For Run C, the anomalous

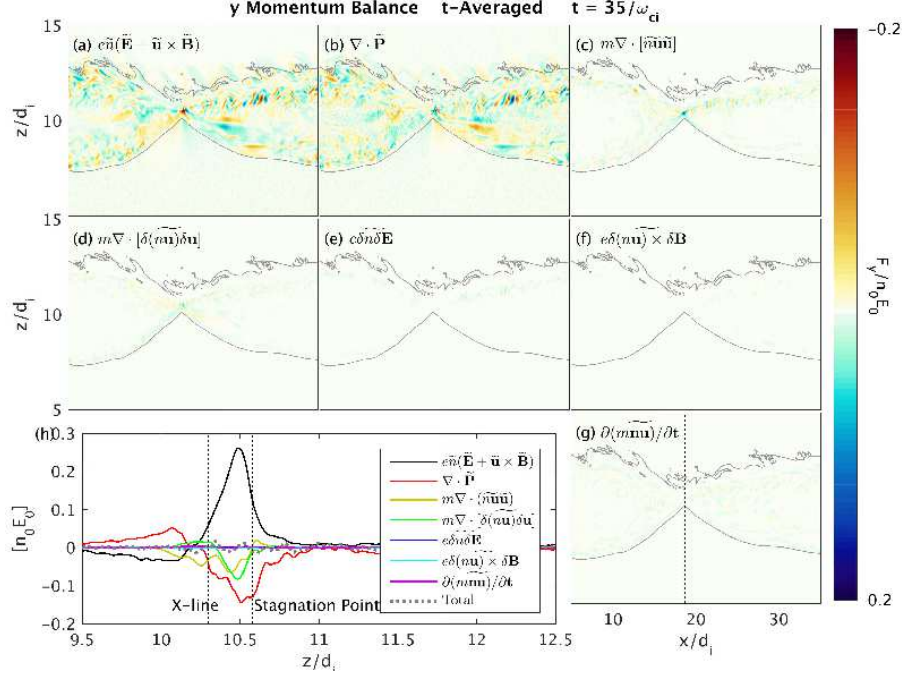


FIG. 16: Terms in the t -averaged Ohm's law contributing to electron momentum balance from Run B with $B_g/B_0 \sim 0.4$. A contribution from the Reynold's stress $\propto \nabla \cdot [m\delta(\overline{n\mathbf{u}})\delta\mathbf{u}]$ appears between the X-line and the stagnation point.

contributions are negligible. Note, however, that the definition of "anomalous" terms here depends on the length of the time averaging interval. Because the interval Δt was shorter than the full lower-hybrid period for Run C, some fluctuations on the lower-hybrid time scale show up in the mean quantities. This likely explains why the terms in Fig. 17 show considerably more fine-scale structure than those in Fig. 16, which used a longer time interval Δt . Unfortunately, we did not test the effect of varying the t -averaging interval when these large calculations were performed. The difficulty in interpreting the results of the averaging, however, do highlight the complications involved in comparing numerical data to spacecraft observations, which necessarily average over the finite cadence of the measuring instruments. MMS data is collected at a high enough cadence that lower-hybrid fluctuations are easily resolved, and direct calculations of the term's in Ohm's Law are therefore more like direct local measurements than averaged ones [45].

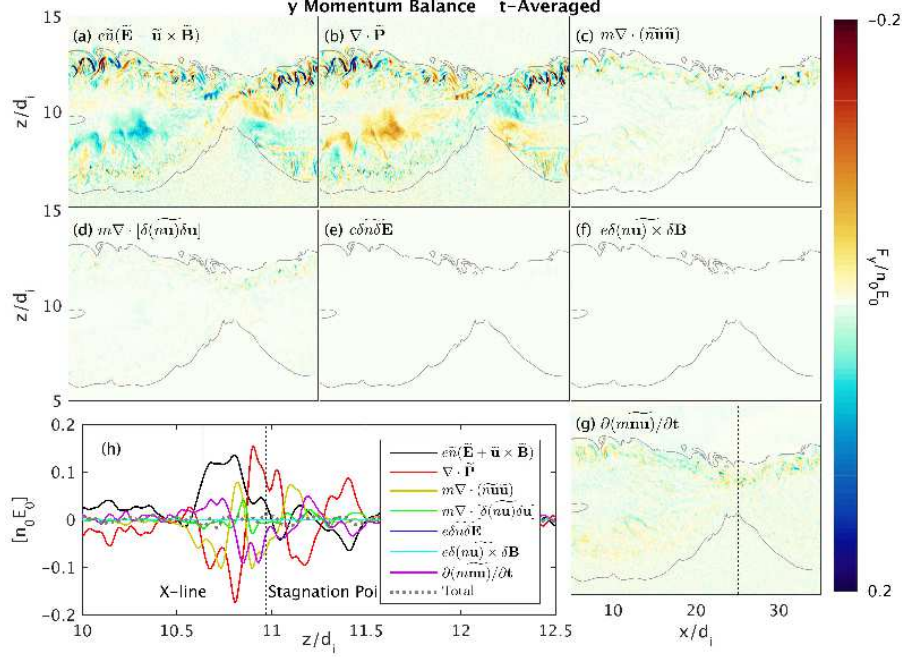


FIG. 17: Terms in the y -averaged Ohm's law contributing to electron momentum balance from Run C with order-unity guide field. The time-averaging interval was here not long enough to cover the entire lower hybrid period, and the strong fluctuations were not completely averaged over. Anomalous terms on this scale were all negligible.

C. Temporal and Field Line tl -Averaging

The time-averaging procedure described in the previous section gives a local measure of anomalous dissipation that is free from potentially misleading problems that can arise in spatial averaging caused by kinking of the current layer. However, the relative importance of various terms may depend upon the chosen location (x - z plane) chosen within the 3D volume. Ideally, we would like to characterize the importance of each physical term in Ohm's law on a field-line basis, and then correlate this understanding with special field lines that pass through the diffusion region or QSL. Furthermore, the simulations do not remain translationally invariant in the out-of-plane y direction, even on average. Thus, while the electric field E_y is the local reconnection electric field at the X-line in 2D systems, other components of the electric field may play this role in a fully 3D system. We seek a diagnostic that does not depend on an initial symmetry direction of the simulation and that could be applied in more realistic 3D systems. A fairly general definition of magnetic reconnection

in 3D is based on the electric field E_{\parallel} parallel to the magnetic field [85]. Under certain conditions, the reconnection rate may be defined as the maximum of the magnetic field line-integrated parallel electric field E_{\parallel} [86–88]. While the assumptions of this theory are not formally satisfied in the periodic slab geometry of our simulations, the peak line-integrated E_{\parallel} has still been found to occur on the field line that passes through the approximate X-line and has a value that agrees with other measures of the reconnection rate.

In light of the above considerations, we consider the component of the electron momentum balance equation in the direction of the magnetic field integrated along field lines. We define the following $t\ell$ -average over time and magnetic field lines:

$$\langle \tilde{\mathbf{V}} \rangle (x_0, y_0, z_0, t_0) = \frac{1}{L} \int_{\mathbf{x}_0}^{\mathbf{x}_f} \tilde{\mathbf{b}} \cdot \tilde{\mathbf{V}}(x, y, z, t_0) dl \quad (12)$$

where $\tilde{\mathbf{b}} = \tilde{\mathbf{B}}/|\tilde{\mathbf{B}}|$ is the unit vector in the direction of the time-averaged magnetic field, and the integral is taken from each initial point \mathbf{x}_0 within the sample plane to a final point \mathbf{x}_f a distance $L = 5d_{i0}$ away along the magnetic field. To test this method, we choose to seed our field line integrator with initial points \mathbf{x}_0 that populate a plane in the x and z directions. In the Appendix, we verify that using the unit vector and fields lines of the time-averaged magnetic field $\tilde{\mathbf{B}}$ does not significantly affect the conclusions of our calculations.

The various terms in the $t\ell$ -averaged Ohm's Law are plotted in Fig. 18 from Run B with $B_g/B_0 \sim 0.4$ and in Fig. 19 from Run C with $B_g/B_0 \sim 1$. While we plot these values in panels (a-g) of each figure at the initial seed points in a plane, each term is really a field-line average that must be associated with an entire magnetic field line. Thus, in the line cuts in panels (h) in each plot, the contributions labeled "X-line" and "Stagnation Point" are not local values assigned to those points, but rather they are average contributions along the magnetic field lines that pass through those special points in our selected seed plane. For Run C in Fig. 19, the anomalous terms are all negligible compared to mean 2D-like terms. For Run B in Fig. 18, there is a contribution from the anomalous Reynold's stress that is comparable to the reconnection electric field. As noted above, this anomalous term oscillates, and its sign depends on the which $x - z$ plane in the 3D volume we select. For this particular plane of seed points, its average value on the field line through the X-line is opposite to the spatially local value found in Fig. 16. Nevertheless, the picture that emerges is consistent with 2D simulations [6, 28]: inertia and the divergence of the pressure tensor dominate between the X-line and the stagnation point.

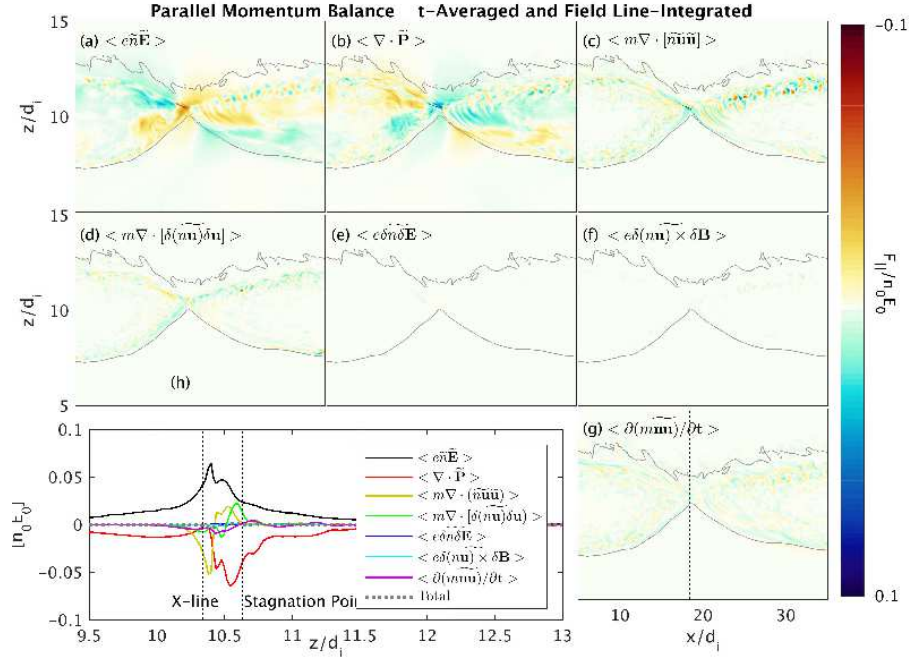


FIG. 18: Terms in the t -averaged and field-line integrated parallel Ohm's law from Run B with $B_g/B_0 \sim 0.4$. The anomalous Reynolds's stress contribution (green curve) is found on average to be opposite that required to balance the global reconnection electric field.

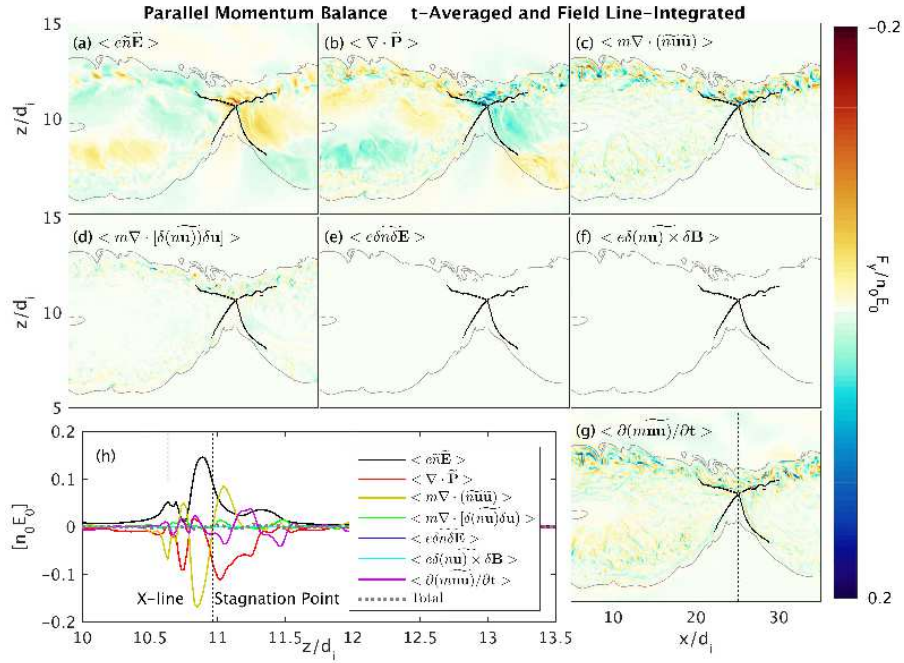


FIG. 19: Terms in the t -averaged and field-line-integrated parallel Ohm's law from Run C with order-unity guide field. Anomalous terms are small.

V. SUMMARY DISCUSSION

Three fully kinetic 3D simulations of asymmetric magnetic reconnection were performed with plasma parameters matching MMS diffusion region encounters. A common feature of all three simulations was the development of lower-hybrid range fluctuations, driven by diamagnetic drifts along the steep density gradient separating magnetosheath and magnetosphere plasmas.

Three methods of measuring the contributions to the Ohm's law of the drift fluctuations were considered. In Table II, we summarize the results for each run employing the y -, t -, and $t\ell$ -averaging measures. Overall, the picture of electron momentum balance is similar to 2D, where inertia and the divergence of the electron pressure tensor may both be important in the region between the X-line and the flow stagnation point [6]. In Run A, a transient burst of anomalous resistivity is found early in the simulation, though this is most likely related to the choice of initial equilibrium current sheet. If spatial y -averaging is employed, the anomalous Lorentz contribution to the viscosity appears important at later time in agreement with Ref. [45]. However, spatial averaging may be problematic when the current sheet undergoes kinking because this will create a broadened averaged profile, while the current sheet may remain thin locally. Indeed, the anomalous viscosity was not consistently observed when the average was taken over shorter spatial intervals in the y -direction, implying it is caused by the longer wavelength kinking of the current sheet rather than the shorter wavelength electrostatic LHDI. The only other evidence of a non-negligible turbulent contribution to the reconnection electric field comes from a Reynold's stress contribution to anomalous viscosity in the intermediate guide field Run B when temporal averaging is used to define fluctuations. This contribution, however, takes both signs depending on the $x - z$ cut plane, and it does not consistently contribute in either direction over the full volume of the simulation. Thus, we did not find any consistent anomalous contributions to the reconnection electric field at the X-line from the short wavelength LHDI. Furthermore, under conditions typical of the magnetopause for the range of guide fields considered, the global reconnection rates observed in our 3D simulations were very close to 2D simulations

In the classic picture, anomalous dissipation arises from small amplitude fluctuations on small spatial scales and fast temporal scales that are well-separated from the global dynamics. These assumptions are not very well satisfied in our reconnection simulations.

TABLE II: Contributions to the averaged Ohm’s Law in each run. Fluctuating contributions are listed in **bold** text. Anomalous Resistivity is abbreviated as **AR**, the Anomalous Lorentz contribution is listed as **AL**, and **RS** refers to the Reynold’s Stress term. For Run A, the t -averaging diagnostic was unavailable. While the non-ideal field typically peaks between the X-line and stagnation points, we indicate which terms are largest at those two points.

Run		y -Average	t -Average	$t\ell$ -Average
A	X-line	Inertia divP (early) AL (late)	×	×
	$B_g/B_0 \sim 0.1$ Stagnation Point	divP AR (early) AL (late)	×	×
B	X-line	Inertia divP	Inertia divP	Inertia
	$B_g/B_0 \sim 0.4$ Stagnation Point	divP	divP (RS)	divP (RS)
C	X-line	Inertia	Inertia divP	Inertia
	$B_g/B_0 \sim 1$ Stagnation Point	divP	Inertia	divP Inertia

This muddies the interpretation of the anomalous dissipation terms, which depend on the choice of averaging scales and procedure. For comparison to spacecraft data, too, it is unclear how best to quantify or identify anomalous dissipation. It has been pointed out that MMS records observations at a high enough cadence that the measurements are essentially localized in time and space [45]. This makes identifying the reconnection rate difficult because the local fluctuating electric fields may be orders of magnitude larger than the global reconnection electric field. Despite the difficulty of this measurement, accounting for all known time-aliasing, spatial-averaging, and instrumental errors, analysis of the Ohm’s law in MMS encounters with diffusion regions have still found that high-frequency or short-wavelength fluctuations may have contributions as large as the resolved terms [24, 89] in the

non-ideal electric field.

While the overall reconnection rates were similar in 2D and 3D, the drift fluctuations along the magnetospheric separatrix produced particle transport across the magnetic field that relaxed the density gradient across the magnetopause [45]. The level of particle transport was found to be in reasonable agreement with estimates from quasi-linear theory as well as diffusion coefficients inferred from MMS observations [32]. A signature of the enhanced particle transport is the presence of cold beams of magnetosheath electrons within the magnetospheric inflow, which were observed by MMS [26] and in our 3D kinetic simulations. In each 3D simulation, there was also enhanced heating of the electrons (compared to 2D simulations) in the parallel direction within the mix layer. In 2D simulations, which limit cross-field particle transport, the inflow electron heating was well-described by CGL-like equations of state [40, 58, 59]. In our 3D simulations and MMS data, however, the electron temperature may decrease even as the density decreases [32, 62]. A complete heating model must account for the mixed magnetosheath electrons as well as the precise heating mechanisms in the mix layer, which are left for future work.

Acknowledgments

A.L. received support from the LDRD office at LANL and acknowledges NASA project NNX14AL38G/NNH17AE36I. W.D.'s work was supported by NASA through the Collaborative Space Weather Modeling Program. Y.-H. L. is supported by NASA grant NNX16AG75G and the MMS mission. Simulations were performed on Trinity at LANL, Blue Waters at the NCSA through project ACI1640768, Pleiades provided by NASA's HEC Program, and LANL Institutional Computing resources.

-
- [1] E. R. Priest and T. G. Forbes, *Astronomy and Astrophysics Review* **10**, 313 (2002), ISSN 0935-4956.
 - [2] M. Yamada, R. Kulsrud, and H. Ji, *Rev. Mod. Phys.* **82**, 603 (2010).
 - [3] F. S. Mozer and P. L. Pritchett, *Geophys. Res. Lett.* **36**, L07102 (2009).
 - [4] D. B. Graham, Y. V. Khotyaintsev, A. Vaivads, M. André, and A. Fazakerley, *Physical Review Letters* **112**, 215004 (2014).

- [5] M. Hesse, N. Aunai, D. Sibeck, and J. Birn, *Geophysical Research Letters* **41**, 8673 (2014).
- [6] M. Hesse, Y.-H. Liu, L.-J. Chen, N. Bessho, M. Kuznetsova, J. Birn, and J. L. Burch, *Geophysical Research Letters* **43**, 2359 (2016).
- [7] T. Moore, J. Burch, W. Daughton, S. Fuselier, H. Hasegawa, S. Petrinec, and Z. Pu, *Journal of Atmospheric and Solar-Terrestrial Physics* **99**, 32 (2013).
- [8] B. Ö. Sonnerup, *Journal of Geophysical Research* **79**, 1546 (1974).
- [9] C. T. Russell and R. C. Elphic, *Geophys. Res. Lett.* **6**, 33 (1979), ISSN 0094-8276, URL <http://dx.doi.org/10.1029/GL006i001p00033>.
- [10] S. Cowley, *Reviews of Geophysics* **20**, 531 (1982).
- [11] J. R. Wygant, R. B. Torbert, and F. Mozer, *Journal of Geophysical Research: Space Physics* **88**, 5727 (1983).
- [12] T. D. Phan, L. M. Kistler, B. Klecker, G. Haerendel, G. Paschmann, B. U. O. Sonnerup, W. Baumjohann, M. B. Bavassano-Cattaneo, C. W. Carlson, A. M. Dilellis, et al., *Nature* **404**, 848 (2000), ISSN 0028-0836.
- [13] F. S. Mozer, S. D. Bale, and T. D. Phan, *Phys. Rev. Lett.* **89**, 015002 (2002), URL <http://link.aps.org/doi/10.1103/PhysRevLett.89.015002>.
- [14] G. Paschmann, I. Papamastorakis, N. Sckopke, G. Haerendel, B. U. O. Sonnerup, S. J. Bame, J. R. Asbridge, J. T. Gosling, C. T. Russel, and R. C. Elphic, *Nature* **282**, 243 (1979).
- [15] P. A. Cassak and M. A. Shay, *Phys. Plasmas* **14** (2007), ISSN 1070-664X.
- [16] J. E. Borovsky and M. Hesse, *Phys. Plasmas* **14** (2007), ISSN 1070-664X.
- [17] F. S. Mozer, P. L. Pritchett, J. Bonnell, D. Sundkvist, and M. T. Chang, *Journal of Geophysical Research (Space Physics)* **113**, A00C03 (2008).
- [18] P. L. Pritchett, *J. Geophys. Res.* **113** (2008), ISSN 0148-0227.
- [19] P. L. Pritchett and F. S. Mozer, *J. Geophys. Res.* **114** (2009), ISSN 0148-0227.
- [20] N. Bessho, L.-J. Chen, and M. Hesse, *Geophysical Research Letters* **43**, 1828 (2016).
- [21] L.-J. Chen, M. Hesse, S. Wang, N. Bessho, and W. Daughton, *Geophysical Research Letters* **43**, 2405 (2016).
- [22] J. Egedal, A. Le, W. Daughton, B. Wetherton, P. Cassak, L.-J. Chen, B. Lavraud, R. Torbert, J. Dorelli, D. Gershman, et al., *Physical review letters* **117**, 185101 (2016).
- [23] M. Shay, T. Phan, C. Haggerty, M. Fujimoto, J. Drake, K. Malakit, P. Cassak, and M. Swisdak, *Geophysical Research Letters* **43**, 4145 (2016).

- [24] R. Torbert, J. Burch, B. Giles, D. Gershman, C. Pollock, J. Dorelli, L. Avanov, M. Argall, J. Shuster, R. Strangeway, et al., *Geophysical Research Letters* **43**, 5918 (2016).
- [25] J. Burch, R. Torbert, T. Phan, L.-J. Chen, T. Moore, R. Ergun, J. Eastwood, D. Gershman, P. Cassak, M. Argall, et al., *Science* **352**, aaf2939 (2016).
- [26] J. Burch and T. Phan, *Geophysical Research Letters* **43**, 8327 (2016).
- [27] S. Zenitani, H. Hasegawa, and T. Nagai, *Journal of Geophysical Research: Space Physics* **122**, 7396 (2017).
- [28] J. Egedal, A. Le, W. Daughton, B. Wetherton, P. Cassak, J. Burch, B. Lavraud, J. Dorelli, D. Gershman, and L. Avanov, *Physical Review Letters* **120**, 055101 (2018).
- [29] R. Davidson and N. Gladd, *The Physics of Fluids* **18**, 1327 (1975).
- [30] W. Daughton, *Phys. Plasmas* **10**, 3103 (2003), ISSN 1070-664X.
- [31] A. Vaivads, M. André, S. Buchert, J.-E. Wahlund, A. Fazakerley, and N. Cornilleau-Wehrin, *Geophysical research letters* **31** (2004).
- [32] D. B. Graham, Y. V. Khotyaintsev, C. Norgren, A. Vaivads, M. André, S. Toledo-Redondo, P.-A. Lindqvist, G. Marklund, R. Ergun, W. Paterson, et al., *Journal of Geophysical Research: Space Physics* **122**, 517 (2017).
- [33] T. Carter, H. Ji, F. Trintchouk, M. Yamada, and R. Kulsrud, *Physical review letters* **88**, 015001 (2001).
- [34] J. Yoo, M. Yamada, H. Ji, J. Jara-Almonte, C. E. Myers, and L.-J. Chen, *Physical review letters* **113**, 095002 (2014).
- [35] J. Yoo, B. Na, J. Jara-Almonte, M. Yamada, H. Ji, V. Roytershteyn, M. R. Argall, W. Fox, and L.-J. Chen, *Journal of Geophysical Research: Space Physics* **122**, 9264 (2017).
- [36] S. Bale, F. Mozer, and T. Phan, *Geophysical research letters* **29** (2002).
- [37] C. Norgren, A. Vaivads, Y. V. Khotyaintsev, and M. André, *Physical review letters* **109**, 055001 (2012).
- [38] R. Treumann, J. LaBelle, and R. Pottetelette, *Journal of Geophysical Research: Space Physics* **96**, 16009 (1991).
- [39] S. P. Gary and A. Sgro, *Geophysical Research Letters* **17**, 909 (1990).
- [40] A. Le, W. Daughton, L.-J. Chen, and J. Egedal, *Geophysical Research Letters* **44**, 2096 (2017).
- [41] J. D. Huba, N. T. Gladd, and K. Papadopoulos, *Geophys. Res. Lett.* **4**, 125 (1977).
- [42] R. Davidson, N. Gladd, C. Wu, and J. Huba, *The Physics of Fluids* **20**, 301 (1977).

- [43] V. Roytershteyn, W. Daughton, H. Karimabadi, and F. S. Mozer, *Phys. Rev. Lett.* **108**, 185001 (2012), URL <http://link.aps.org/doi/10.1103/PhysRevLett.108.185001>.
- [44] L. Price, M. Swisdak, J. Drake, P. Cassak, J. Dahlin, and R. Ergun, *Geophysical Research Letters* **43**, 6020 (2016).
- [45] L. Price, M. Swisdak, J. Drake, J. Burch, P. Cassak, and R. Ergun, *Journal of Geophysical Research: Space Physics* (2017).
- [46] H. Che, J. Drake, and M. Swisdak, *Nature* **474**, 184 (2011).
- [47] L.-J. Chen, M. Hesse, S. Wang, D. Gershman, R. Ergun, J. Burch, N. Bessho, R. Torbert, B. Giles, J. Webster, et al., *Journal of Geophysical Research: Space Physics* (2017).
- [48] K. J. Bowers, B. J. Albright, L. Yin, B. Bergen, and T. J. T. Kwan, *Physics of Plasmas* **15**, 055703 (pages 7) (2008), URL <http://link.aip.org/link/?PHP/15/055703/1>.
- [49] T. Nakamura, S. Eriksson, H. Hasegawa, S. Zenitani, W. Li, K. Genestreti, R. Nakamura, and W. Daughton, *Journal of Geophysical Research: Space Physics* **122** (2017).
- [50] W. Daughton, T. Nakamura, H. Karimabadi, V. Roytershteyn, and B. Loring, *Physics of Plasmas* **21**, 052307 (2014).
- [51] H. Che, *Physics of Plasmas* **24**, 082115 (2017), <http://dx.doi.org/10.1063/1.5000071>, URL <http://dx.doi.org/10.1063/1.5000071>.
- [52] D. Winske, V. Thomas, and N. Omidi, *Physics of the Magnetopause* pp. 321–330 (1995).
- [53] D. Winske and P. Liewer, *The Physics of Fluids* **21**, 1017 (1978).
- [54] E. R. Priest and P. Démoulin, *Jour. Geophys. Res.* **100**, 23443 (1995).
- [55] V. S. Titov, G. Hornig, and P. Démoulin, *Journal of Geophysical Research: Space Physics* **107** (2002).
- [56] D. Borgogno, D. Grasso, F. Pegoraro, and T. Schep, *Physics of Plasmas* **18**, 102307 (2011).
- [57] Y.-H. Liu, M. Hesse, P. Cassak, M. Shay, S. Wang, and L.-J. Chen, arXiv preprint arXiv:1711.06708 (2017).
- [58] A. Le, J. Egedal, W. Daughton, W. Fox, and N. Katz, *Phys. Rev. Lett.* **102**, 085001 (2009), ISSN 0031-9007.
- [59] J. Egedal, A. Le, P. L. Pritchett, and W. Daughton, *Physics of Plasmas* **18**, 102901 (pages 8) (2011), URL <http://link.aip.org/link/?PHP/18/102901/1>.
- [60] J. Egedal, A. Le, and W. Daughton, *Phys. Plasmas* **20** (2013), ISSN 1070-664X.
- [61] G. F. Chew, M. L. Goldberger, and F. E. Low, *Proc. Royal Soc. A* **112**, 236 (1956).

- [62] S. Wang, L.-J. Chen, M. Hesse, L. B. Wilson, N. Bessho, D. J. Gershman, R. E. Ergun, T. D. Phan, J. L. Burch, J. C. Dorelli, et al., *Geophysical Research Letters* (2017).
- [63] E. N. Parker, *J. Geophys. Res.* **62**, 509 (1957).
- [64] P. H. Yoon and A. T. Lui, *Journal of Geophysical Research: Space Physics* **112** (2007).
- [65] R. G. Kleva, J. F. Drake, and F. L. Waelbroeck, *Phys. Plasmas* **2**, 23 (1995), ISSN 1070-664X.
- [66] Z. Ma and A. Bhattacharjee, *Geophysical research letters* **23**, 1673 (1996).
- [67] D. Biskamp, E. Schwarz, and J. F. Drake, *Phys. Plasmas* **4**, 1002 (1997), ISSN 1070-664X.
- [68] M. M. Kuznetsova, M. Hesse, and D. Winske, *Journal of Geophysical Research: Space Physics* (1978–2012) **106**, 3799 (2001).
- [69] J. Birn, J. F. Drake, M. A. Shay, B. N. Rogers, R. E. Denton, M. Hesse, M. Kuznetsova, Z. W. Ma, A. Bhattacharjee, A. Otto, et al., *J. Geophys. Res.* **106**, 3715 (2001), ISSN 0148-0227.
- [70] W. Daughton, J. Scudder, and H. Karimabadi, *Phys. Plasmas* **13**, 072101 (2006), ISSN 1070-664X.
- [71] P. Cassak, J. Drake, M. Shay, and B. Eckhardt, *Physical review letters* **98**, 215001 (2007).
- [72] M. Ozaki, T. Sato, R. Horiuchi, and C. S. Group, *Physics of Plasmas* **3**, 2265 (1996).
- [73] M. Tanaka and T. Sato, *Journal of Geophysical Research: Space Physics* **86**, 5541 (1981).
- [74] R. Kulsrud, H. Ji, W. Fox, and M. Yamada, *Phys. Plasmas* **12**, 082301 (2005), ISSN 1070-664X.
- [75] N. Krall, *The Physics of Fluids* **20**, 311 (1977).
- [76] J. Brackbill, D. Forslund, K. Quest, and D. Winske, *The Physics of fluids* **27**, 2682 (1984).
- [77] P. Pritchett, F. Coroniti, and V. Decyk, *Journal of Geophysical Research: Space Physics* **101**, 27413 (1996).
- [78] G. Lapenta and J. Brackbill, *Physics of Plasmas* **9**, 1544 (2002).
- [79] W. Daughton, G. Lapenta, and P. Ricci, *Physical review letters* **93**, 105004 (2004).
- [80] I. Silin, J. Büchner, and A. Vaivads, *Physics of plasmas* **12**, 062902 (2005).
- [81] H. T. Ji, S. Terry, M. Yamada, R. Kulsrud, A. Kuritsyn, and Y. Ren, *Phys. Rev. Lett.* **92**, 115001 (2004), ISSN 0031-9007.
- [82] W. Fox, M. Porkolab, J. Egedal, N. Katz, , and A. Le, *Phys. Plasmas* **17**, 072303 (2010).
- [83] V. Roytershteyn, S. Dorfman, W. Daughton, H. Ji, M. Yamada, and H. Karimabadi, *Physics of Plasmas* **20**, 061212 (2013), URL <http://scitation.aip.org/content/aip/journal/pop/20/6/10.1063/1.4811371>.

- [84] S. Dorfman, H. Ji, M. Yamada, J. Yoo, E. Lawrence, C. Myers, and T. Tharp, *Geophysical Research Letters* **40**, 233 (2013).
- [85] K. Schindler, M. Hesse, and J. Birn, *Jour. Geophys. Res.* **93**, 5547 (1988).
- [86] M. Hesse and J. Birn, *Advances in Space Research* **13**, 249 (1993).
- [87] Y.-H. Liu, M. Hesse, and M. Kuznetsova, *Journal of Geophysical Research: Space Physics* **120**, 7331 (2015).
- [88] J. P. Sauppe and W. Daughton, *Physics of Plasmas* **25**, 012901 (2018).
- [89] R. Torbert, J. Burch, M. Argall, L. Alm, C. Farrugia, T. Forbes, B. Giles, A. Rager, J. Dorelli, R. Strangeway, et al., *Journal of Geophysical Research: Space Physics* (2017).